Competing anticlastic and piezoelectric deformation at large deflections

OPEN ACCESS
IOP Publishing
Smart Materials and Structures
Smart Mater. Struct. **30** (2021) 035019 (16pp)
https://doi.org/10.1088/1361-665X/abdcfd

Competing anticlastic and piezoelectric deformation at large deflections

H Salmani, U Hanke and E Halvorsen

Department of Microsystems, University of South-Eastern Norway, Campus Vestfold, Horten, Norway

E-mail: Einar.Halvorsen@usn.no

Received 12 October 2020, revised 7 December 2020
Accepted for publication 18 January 2021
Published 5 February 2021

Abstract

In bending of a purely elastic beam or plate, it is well established that the cross-sectional shape changes character with decreasing bending radius-of-curvature and that the transition can be characterized by the Searle parameter. In a piezoelectric structure, the cross-sectional deformation is affected by the opposite anticlastic and electromechanical bending curvatures. The behavior is consequently more complicated and it is an open question how the cross-sectional shape develops with increasing bending. In this paper, analytical solutions are used to study the cross-sectional deformation of piezoelectric cantilever-actuators taking both anticlastic and electromechanical bending effects into account. We consider unimorph and bimorph actuators. In the case of electrical actuation, as for the purely mechanical case, we find that the Searle parameter is an important parameter characterizing the shape of the cross-section. A load scaling rule gives a criterion for fixed cross-section-deflection for different actuator widths. Using this scaling rule, the Searle parameter is kept unchanged. The analytical results are verified by non-linear finite element analysis using electric potential and mechanical moment as applied loads.

Keywords: piezoelectricity, anticlastic curvature, Searle parameter, actuator, beam, bender, large deflections

1. Introduction

Anticlastic deformation is the phenomenon that for a beam or plate, curvature along the width direction is induced by bending along the length direction due to the existence of Poisson's ratio [1]. Increasing the width or decreasing the bending radius-of-curvature leads to neutralization of the anticlastic curvature of the cross section except at the edges [2–4]. This transition corresponds to increasing the Searle parameter b^2/Rt which combines radius of curvature R, width b and thickness t. Since this is a change in behavior arising for large deformations it is an example of a non-linear effect in bending. The anticlastic deformation of the cross-section of an elastic structure and its neutralization formulated by Ashwell [3] was experimentally observed in a beam by Bellow *et al* [5]. After that, the anticlastic deformation in the presence of mechanical loading was studied using analytical, numerical and experimental methods [6–11].

While the limiting cases of narrow and wide beams both can be treated by one-dimensional Euler–Bernoulli theory differing only in flexural rigidity, intermediate cases require some elements of plate theory and authors differ in naming these structures plates or beams [4, 10, 12]. We will simply refer all these cases as structures in the remainder of this paper.

For structures including piezoelectric layers for sensing or actuation, the plane strain and plane stress assumptions are typically made to find the bending deformation of wide and narrow beams, respectively [13–17]. However, the cross-sectional deformation is more complex than the extreme plane stress and strain assumptions predict. While

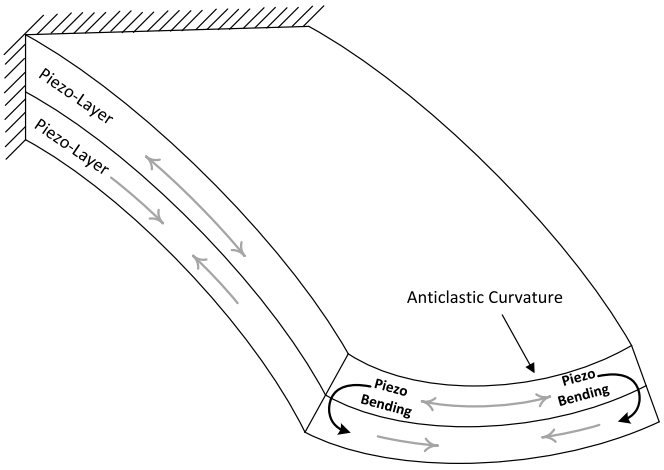

Figure 1. Opposite effects of the anticlastic curvature and the piezoelectric bending moment in the cross section.

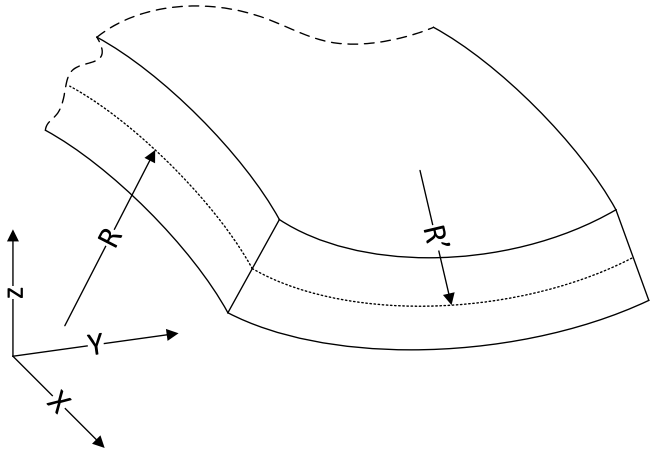

Figure 2. Longitudinal (R) and anticlastic (R') radius-of-curvature.

applying an electric field, the structure is bent longitudinally and the anticlastic deformation is induced because of the Poisson effect. In addition, the same electromechanical bending moment is normally present along the width due to the symmetry of piezoelectric material. This effect is opposite to the anticlastic deformation. Therefore, the total cross-sectional deformation is a result of two opposing deformations. Figure 1 shows how the piezoelectric bending moment acts against the tendency of anticlastic curvature in a bimorph actuator.

Using the effective material coefficients, beam theory gives accurate results for longitudinal deformation in the ideal plane stress and plane strain cases where the Poisson's effect is included [17–19]. There is no analytical solution for actuators in intermediate cases between these two extreme limits even though it is needed. For example, in [20] it was found that the plane stress or plane strain assumptions are not accurate if the width to thickness ratio is between 10 and 1000.

The wider piezoelectric structures with high width/length ratios are extensively used in microactuators [17, 18], microsensors [15] and energy harvesting [21–24]. The transition from narrow to wide orthotropic non-piezoelectric beam was studied by Swanson [6] using the linear plate equations, where the effect of width/length ratio on the cross-section deformation was investigated. The deformation was affected by the width/length ratio because of the boundary conditions at the ends of the structure. This is to be expected from Saint-Venant's principle [25] and is a different effect from the anticlastic deformation studied by Ashwell [3] which is a nonlinear effect of a beam in pure bending.

Since there is no realistic estimation of the cross section deformation of a piezoelectric cantilever actuator in the literature, an analytical solution is developed in this paper to predict the deformation of the cross section. To this end, we have generalized Ashwell's results [3] to a piezoelectric actuator. We use the energy method for deriving the more general equations as we find it conceptually simpler and more suitable for generalization than Ashwell's force balance argument. We consider bending due to a mechanical bending moment and an electrical voltage across the electrodes. The effects on the cross-section deformation are studied and verified by finite element (FE) analysis. To this end we compare to the cross section in the middle of a long structure to secure that the result is not affected by the boundary conditions. In the final section, the effect of the Searle parameter is studied in a multi-layer actuator. While the shape of the cross-section depends on the combination of mechanical loading and electrical actuation we show that it is possible to find a scaling relation between the two which keeps the shape of the cross-section fixed when the width is varied at constant Searl parameter.

2. Analytical solution

The bending and anticlastic curvatures of a rectangular cross section structure are shown schematically in figure 2, where R and R' are the bending and anticlastic radius-of-curvatures, respectively. For an arbitrary layered structure including piezoelectric layers, applying a voltage will result in longitudinal deformation u and bending radius-of-curvature R as well as the cross section deformation v and w in the plane of cross section. The cross section deformation is depicted in figure 3.

In order to deal with the deflection along the transversal direction, it is necessary to use plate theory. Assuming a constant bending radius-of-curvature, small strain and allowing large displacement of the axis, the normal strains are defined by modifying the linear classical plate theory as follows:

$$S_1 = u_{,x}(x) - \frac{(z - z_0) + w(y)}{R(x)}, \tag{1}$$

$$S_2 = v_{,y}(y) - (z - z_0)\, w_{,yy}(y). \tag{2}$$

See the appendix A for details. The loading conditions, i.e. tip bending moment and position independent voltage actuation, dictate that $u_{,x}$ and R both are position independent.

To find the stresses T, the linear constitutive equations [26]

$$T_{ij} = C^E_{ijkl} S_{kl} - e_{kij} E_k$$
$$D_i = e_{ikl} S_{kl} + \varepsilon^S_{ik} E_k \tag{3}$$

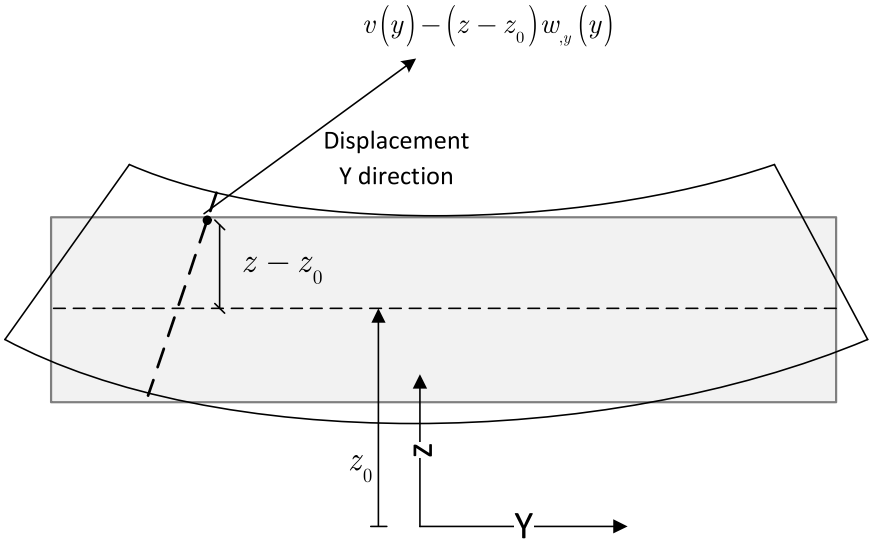

Figure 3. Cross section deformation by assuming small displacement within the cross section.

are used. In equation (3) the material parameters C^E_{ijkl}, e_{kij} and ε^S_{ik} are mechanical stiffness, stress piezoelectric coefficient, and permittivity at constant strain, respectively. D_i and E_k are the electric displacement and the electric field of the piezoelectric material, respectively.

The material parameterization in equation (3) is reformulated for a piezoelectric plate in terms of in-plane strains and tractions on horizontal surfaces. Making thin-plate assumptions, we then neglect traction on horizontal surfaces, all shear stresses and all shear strains. This is standard thin-plate theory [14, 27]. It means that the thickness must be significantly smaller than both the transversal and longitudinal dimensions. How much depends on the need for accuracy, but a ratio of 1/20 has been practiced as a rule of the thumb [28]. We treat in-plane electric fields as zero and will also neglect fringing fields at the edges. This requires the lateral dimensions to be significantly larger than the thickness of the piezoelectric layer. In conclusion, we obtain the simplified constitutive equations

$$\begin{Bmatrix} T_1 \\ T_2 \end{Bmatrix} = \begin{bmatrix} C^*_{11} & C^*_{12} \\ C^*_{12} & C^*_{11} \end{bmatrix} \begin{Bmatrix} S_1 \\ S_2 \end{Bmatrix} - \begin{Bmatrix} e^*_{31} \\ e^*_{31} \end{Bmatrix} E_3$$
$$D_3 = \begin{bmatrix} e^*_{31} & e^*_{31} \end{bmatrix} \begin{Bmatrix} S_1 \\ S_2 \end{Bmatrix} + \varepsilon^{*S}_{33} E_3. \tag{4}$$

The asterisk denotes effective material properties [13, 14, 29].

We consider a structure of n layers where layer number $k \in \{1, 2, \ldots, n\}$ extends from $z = z^{k-1}$ to $z = z^k$. Further assuming constant electric potential along the length, constant D_3, and using $\int_{z^{k-1}}^{z^k} E^k_3 dz = V^k$ for the voltage across the layer, the electric field E^k_3 and electric displacement D^k_3 of the kth layer are rewritten as a function of voltage and strain as:

$$D^k_3 = -\varepsilon^{*Sk}_{33}\frac{V^k}{h^k} + \begin{bmatrix} e^{*k}_{31} & e^{*k}_{31} \end{bmatrix} \left[\frac{1}{h^k} \int_{z^{k-1}}^{z^k} \begin{Bmatrix} S_1 \\ S_2 \end{Bmatrix} dz \right] \tag{5}$$

$$E^k_3 = -\frac{V^k}{h^k} - \frac{\begin{bmatrix} e^{*k}_{31} & e^{*k}_{31} \end{bmatrix}}{\varepsilon^{*Sk}_{33}} \left[\begin{Bmatrix} S_1 \\ S_2 \end{Bmatrix} - \frac{1}{h^k} \int_{z^{k-1}}^{z^k} \begin{Bmatrix} S_1 \\ S_2 \end{Bmatrix} dz \right] \tag{6}$$

where $h^k = z^k - z^{k-1}$ is the the thickness of the kth layer. Substituting equations (5) and (6) into the equation (4), the mechanical stresses induced by the voltage at the corresponding layer are given by

$$T^k_1 = C^{*k}_{11} S_1 + C^{*k}_{12} S_2 + e^{*k}_{31}\frac{V^k}{h^k} + \frac{{e^{*k}_{31}}^2}{\varepsilon^{*Sk}_{33}} \left(S_1 - \frac{1}{h^k}\int_{z^{k-1}}^{z^k} S_1 dz \right)$$
$$+ \frac{{e^{*k}_{31}}^2}{\varepsilon^{*Sk}_{33}} \left(S_2 - \frac{1}{h^k}\int_{z^{k-1}}^{z^k} S_2 dz \right) \tag{7}$$

and

$$T^k_2 = C^{*k}_{12} S_1 + C^{*k}_{11} S_2 + e^{*k}_{31}\frac{V^k}{h^k} + \frac{{e^{*k}_{31}}^2}{\varepsilon^{*Sk}_{33}} \left(S_1 - \frac{1}{h^k}\int_{z^{k-1}}^{z^k} S_1 dz \right)$$
$$+ \frac{{e^{*k}_{31}}^2}{\varepsilon^{*Sk}_{33}} \left(S_2 - \frac{1}{h^k}\int_{z^{k-1}}^{z^k} S_2 dz \right). \tag{8}$$

Finding the governing differential equations considering both curvatures due to the applied voltage and anticlastic deformation is achieved by employing the energy method. For this purpose, the electric enthalpy of a piezoelectric structure [30] is simplified using thin-plate assumptions and integrated over the undeformed configuration volume [31] as:

$$H = \frac{1}{2}\int_V (T_1 S_1 + T_2 S_2 - D_3 E_3)\, dV. \tag{9}$$

Substituting the equations (5)–(8) into equation (9) gives electric enthalpy in terms of strain as

$$H=\sum_{k=1}^{n}\int_{0}^{L}\int_{-b/2}^{b/2}\int_{z^{k-1}}^{z^{k}}\left(\frac{1}{2}\begin{bmatrix} S_1 & S_2 & \bar{S}_1 & \bar{S}_2 \end{bmatrix}\begin{bmatrix} C_{11}^{*k}+\frac{e_{31}^{*k^2}}{\varepsilon_{33}^{*Sk}} & C_{12}^{*k}+\frac{e_{31}^{*k^2}}{\varepsilon_{33}^{*Sk}} & 0 & 0 \\ C_{12}^{*k}+\frac{e_{31}^{*k^2}}{\varepsilon_{33}^{*Sk}} & C_{11}^{*k}+\frac{e_{31}^{*k^2}}{\varepsilon_{33}^{*Sk}} & 0 & 0 \\ 0 & 0 & -\frac{e_{31}^{*k^2}}{h^{k^2}\varepsilon_{33}^{*Sk}} & -\frac{e_{31}^{*k^2}}{h_k{}^2\varepsilon_{33}^{*Sk}} \\ 0 & 0 & -\frac{e_{31}^{*k^2}}{h^{k^2}\varepsilon_{33}^{*Sk}} & -\frac{e_{31}^{*k^2}}{h^{k^2}\varepsilon_{33}^{*Sk}} \end{bmatrix}\right.$$
$$\left.+2\frac{V^k e_{31}^{*k}}{h^{k^2}}\begin{bmatrix} 0 & 0 & 1 & 1 \end{bmatrix}\right)\begin{Bmatrix} S_1 \\ S_2 \\ \bar{S}_1 \\ \bar{S}_2 \end{Bmatrix}-e_{31}^{*k}\left(\frac{V^k}{h^k}\right)^2\Bigg)dxdyz \tag{10}$$

where b and L are respectively the width and length of the structure, $\bar{S}_1=\int_{z^{k-1}}^{z^k}S_1dz$ and $\bar{S}_2=\int_{z^{k-1}}^{z^k}S_2dz$. For the static problem, the kinetic energy part of the Lagranian is zero and Hamilton's principle is reduced to

$$\delta\left(H-W_e\right)=0 \tag{11}$$

where W_e is the external work done by the applied bending moment M_n at the tip of the structure. Substituting equations (1), (2) and (10) into the variation of equation (11) and equating the coefficients of variations $\delta\frac{1}{R}$, $\delta u_{,x}$, $\delta w\left(y\right)$ and $\delta v_{,y}\left(y\right)$ to zero gives four coupled equations as:

$$K_{11}bu_{,x}-\frac{1}{R}\left(b\overline{K}_{11}+K_{11}\int_{-b/2}^{+b/2}w\left(y\right)dy\right)$$
$$+K_{12}\int_{-b/2}^{+b/2}v_{,y}\left(y\right)dy-\overline{K}_{12}\int_{-b/2}^{+b/2}w_{,yy}\left(y\right)dy+P_EbV=0, \tag{12}$$

$$M_n-\left(M_Eb+P_E\int_{-b/2}^{b/2}w\left(y\right)dy\right)V$$
$$-\left(b\overline{K}_{11}+K_{11}\int_{-b/2}^{b/2}w\left(y\right)dy\right)u_{,x}$$
$$-\frac{1}{R}\left(bK_\xi-b\overline{\overline{K}}_{11}-2\overline{K}_{11}\int_{-b/2}^{b/2}w\left(y\right)dy-K_{11}\int_{-b/2}^{b/2}w^2\left(y\right)dy\right)$$
$$-\left(K_\xi-\overline{\overline{K}}_{12}\right)\int_{-b/2}^{b/2}w_{,yy}\left(y\right)dy-\overline{K}_{12}\int_{-b/2}^{b/2}v_{,y}\left(y\right)dy$$
$$-K_{12}\int_{-b/2}^{b/2}w\left(y\right)v_{,y}\left(y\right)dy+\overline{K}_{12}\int_{-b/2}^{b/2}w\left(y\right)w_{,yy}\left(y\right)dy=0, \tag{13}$$

$$\left(\overline{\overline{K}}_{11}-K_{2,\xi}\right)R^2\frac{d^4w\left(y\right)}{dy^4}+2R\overline{K}_{12}\frac{d^2w\left(y\right)}{dy^2}+K_{11}w\left(y\right)$$
$$-\overline{K}_{11}R^2\frac{d^2v_{,y}\left(y\right)}{dy^2}-RK_{12}v_{,y}\left(y\right)-VRP_E+P_{11,M}=0, \tag{14}$$

$$-\overline{K}_{11}R\frac{d^2w\left(y\right)}{dy^2}-K_{12}w\left(y\right)$$
$$+K_{11}Rv_{,y}\left(y\right)+VRP_E-P_{12,M}=0. \tag{15}$$

The coefficients of equations (12)–(15) are given by:

$$K_{11}=\sum_{k=1}^{n}C_{11}^{*k}h^k \tag{16}$$

$$K_{12}=\sum_{k=1}^{n}C_{12}^{*k}h^k \tag{17}$$

$$\overline{K}_{11}=\sum_{k=1}^{n}C_{11}^{*k}h_1^k \tag{18}$$

$$\overline{K}_{12}=\sum_{k=1}^{n}C_{12}^{*k}h_1^k \tag{19}$$

$$\overline{\overline{K}}_{11}=\sum_{k=1}^{n}C_{11}^{*k}h_2^k \tag{20}$$

$$\overline{\overline{K}}_{12}=\sum_{k=1}^{n}C_{12}^{*k}h_2^k \tag{21}$$

$$K_\xi=\sum_{k=1}^{n}\frac{e_{31}^{*k^2}}{\varepsilon_{33}^{*Sk}}\left(\frac{h_1^k{}^2}{h^k}-h_2^k\right) \tag{22}$$

$$P_E=\sum_{k=1}^{n}e_{31}^{*k}\hat{V}^k \tag{23}$$

$$M_E=\sum_{k=1}^{n}e_{31}^{*k}\frac{h_1^k}{h^k}\hat{V}^k \tag{24}$$

$$P_{11,M}=\overline{K}_{11}-K_{11}Ru_{,x} \tag{25}$$

and

$$P_{12,M}=\overline{K}_{12}-K_{12}Ru_{,x}. \tag{26}$$

where $h_1^k = \int_{z^{k-1}}^{z^k} (z - z_0)\,\mathrm{d}z$ and $h_2^k = \int_{z^{k-1}}^{z^k} (z - z_0)^2 \mathrm{d}z$ are geometric parameters. In equations (23) and (24), $\hat{V}^k = V^k/V$ and V is the applied voltage at a reference piezoelectric layer. K_ξ in equation (22) represents the electromechanical coupling.

Equation (11) provides us with two boundary conditions corresponding to the shear force and bending moment at the edge. These are

$$\left[\left(\overline{\overline{K}}_{11} - K_\xi\right) R\frac{d^2w(y)}{dy^2} + \overline{K}_{12} w(y) - \overline{K}_{11} R v_{,y}(y) - K_\xi + \overline{P}_{12,M} - VRM_E\right]\Big|_{y=\pm\frac{b}{2}} = 0 \tag{27}$$

and

$$\left[\left(\overline{\overline{K}}_{11} - K_\xi\right) R\frac{d^3w(y)}{dy^3} + \overline{K}_{12}\frac{dw(y)}{dy} - K_{11} R\frac{dv_{,y}(y)}{dy}\right]\Big|_{y=\pm\frac{b}{2}} = 0 \tag{28}$$

where the mechanical moment $\overline{P}_{12,M}$ is

$$\overline{P}_{12,M} = \overline{\overline{K}}_{12} - \overline{K}_{12} R u_{,x}. \tag{29}$$

By solving equation (15) for $v_{,y}(y)$ to obtain

$$v_{,y}(y) = \frac{\overline{K}_{11}}{K_{11}}\frac{d^2w(y)}{dy^2} + \frac{K_{12}}{K_{11}R} w(y) - \frac{V}{K_{11}} P_E + \frac{1}{K_{11}R} P_{12,M} \tag{30}$$

and substituting it in equation (14), the coupled differential equations are converted to a single ordinary differential equation for the function $w(y)$:

$$D_{11}R^2\frac{d^4w(y)}{dy^4} + 2D_{12}R\frac{d^2w(y)}{dy^2} + D_{22} w(y) + P_T = 0 \tag{31}$$

in which the coefficients are given by

$$D_{11} = \left(\overline{\overline{K}}_{11} - K_\xi - \frac{\overline{K}_{11}^{\,2}}{K_{11}}\right), \tag{32}$$

$$D_{12} = \left(\overline{K}_{12} - \frac{\overline{K}_{11} K_{12}}{K_{11}}\right), \tag{33}$$

$$D_{22} = \left(K_{11} - \frac{K_{12}^{\,2}}{K_{11}}\right), \tag{34}$$

and

$$P_T = VR\left(\frac{K_{12}}{K_{11}} - 1\right) P_E - \frac{K_{12}}{K_{11}} P_{12,M} + P_{11,M}. \tag{35}$$

Using the same procedure, the coupled boundary conditions of equations (27) and (28) are converted to the equations

$$\left[D_{11}R\frac{d^2w(y)}{dy^2} + D_{12} w(y) + M_T\right]\Big|_{y=\pm\frac{b}{2}} = 0 \tag{36}$$

and

$$\left[D_{11}R\frac{d^3w(y)}{dy^3} + D_{12}\frac{dw(y)}{dy}\right]\Big|_{y=\pm\frac{b}{2}} = 0 \tag{37}$$

where

$$M_T = VR\left(\frac{\overline{K}_{11}}{K_{11}} P_E - M_E\right) - \frac{\overline{K}_{11}}{K_{11}} P_{12,M} + \overline{P}_{12,M} - K_\xi. \tag{38}$$

Based on the coefficients of the ordinary differential equation (31), the roots of the characteristic equation are given by

$$\beta_j = \sqrt{\frac{-D_{12} \pm \sqrt{{D_{12}}^2 - D_{11}D_{22}}}{RD_{11}}}, j = 1..4. \tag{39}$$

The β_js can be real, imaginary or complex values but physically only one of them is feasible. In order to find the physically possible values of β_j, the enthalpy equation (10) is rewritten in quadratic form by substituting $v_{,y}$ from equation (30) as

$$H = \frac{1}{2}\begin{bmatrix} \frac{d^2w(y)}{dy^2} \\ w(y) \end{bmatrix}^T \underbrace{\begin{bmatrix} D_{11}R^2 & D_{12}R \\ D_{12}R & D_{22} \end{bmatrix}}_{D} \begin{bmatrix} \frac{d^2w(y)}{dy^2} \\ w(y) \end{bmatrix} + \begin{bmatrix} \left(\frac{\overline{K}_{11}}{K_{11}} P_e - M_e\right) VR^2 - \frac{\overline{K}_{11}}{K_{11}} P_{12,M} + R\left(\hat{M}_M - K_\xi\right) \\ P_T \end{bmatrix}^T \times \begin{bmatrix} \frac{d^2w(y)}{dy^2} \\ w(y) \end{bmatrix} + \hat{H}_o, \tag{40}$$

where $\hat{H}_o$ is an inconsequential constant term. Based on the equation (40), the stability of the system is achieved if the matrix $[D]$ is positive definite. Therefore $D_{11}R^2$, D_{22}, and the determinant of the $[D]$ matrix $R^2\left(D_{11}D_{22} - D_{12}^2\right)$ must be positive values. The bending radius-of-curvature R is a real value, therefore the stability requires the condition $D_{11}D_{22} > D_{12}^2$ which means $\sqrt{D_{12}^2 - D_{11}D_{22}}$ is an imaginary number. Consequently, β_j, $j = 1..4$, is simplified to the complex values $\pm\alpha_1 \pm i\alpha_2$ with manifest real and imaginary parts. Therefore, the possible solutions of the differential equation (31) are on the form

$$w(y) = C_1 \sinh(\alpha_1 y)\sin(\alpha_2 y) + C_2 \cosh(\alpha_1 y)\cos(\alpha_2 y) + C_3 \sinh(\alpha_1 y)\cos(\alpha_2 y) + C_4 \cosh(\alpha_1 y)\sin(\alpha_2 y) - \frac{P_T}{D_{22}}. \tag{41}$$

By applying the boundary conditions (36) and (37), the coefficients can be calculated as

$$C_1 = -M_0\frac{C_1^U}{C^L} \tag{42}$$

and

$$C_2 = M_0\frac{C_2^U}{C^L} \tag{43}$$

where

$$M_0 = \frac{D_{12}}{D_{22}} P_T - M_T, \tag{44}$$

$$C_1^U = A_2 \cosh\left(\alpha_1 \frac{b}{2}\right) \sin\left(\alpha_2 \frac{b}{2}\right) + A_1 \sinh\left(\alpha_1 \frac{b}{2}\right) \cos\left(\alpha_2 \frac{b}{2}\right), \tag{45}$$

$$C_2^U = A_1 \cosh\left(\alpha_1 \frac{b}{2}\right) \sin\left(\alpha_2 \frac{b}{2}\right) - A_2 \sinh\left(\alpha_1 \frac{b}{2}\right) \cos\left(\alpha_2 \frac{b}{2}\right), \tag{46}$$

$$C_L = \frac{1}{2}\left(A_1 A_3 + A_2 A_4\right) \cosh\left(\alpha_1 b\right) \sin\left(\alpha_2 b\right) + \frac{1}{2}\left(A_1 A_4 - A_2 A_3\right) \sinh\left(\alpha_1 b\right) \cos\left(\alpha_2 b\right) \tag{47}$$

and $C_3 = C_4 = 0$. In equations (45)–(47) the coefficients A_i, $i = 1..4$ are

$$A_1 = \alpha_1 \left[RD_{11}\left({\alpha_1}^2 - 3{\alpha_2}^2\right) + D_{12}\right], \tag{48}$$

$$A_2 = \alpha_2 \left[RD_{11}\left({\alpha_2}^2 - 3{\alpha_1}^2\right) - D_{12}\right], \tag{49}$$

$$A_3 = RD_{11}\left({\alpha_1}^2 - {\alpha_2}^2\right) + D_{12} \tag{50}$$

and

$$A_4 = 2RD_{11}\alpha_1\alpha_2. \tag{51}$$

The solution given by equation (41) is a generalization of Ashwell's result [3] to a piezoelectric including all electromechanical parameters. Only in the special case of an elastic single-layered structure with a mechanical loading, the current and Ashwell's [3] solution are identical.

For a given tip bending moment and actuation voltage, the structure axis is bent into an arc with radius-of-curvature R along the longitudinal direction. The radius-of-curvature can not be calculated directly, as it is coupled to the other parameters $w(y)$, $v_{,y}(y)$ and $u_{,x}$. In order to find the solution for the radius of curvature R and the cross section deformation $w(y)$, the system of non-linear equations (12), (13), (30), and (41), including $w(y)$, $v_{,y}(y)$, $u_{,x}$ and R should be solved. For this purpose, an iterative solution is employed, in which equations (12) and (13) are solved neglecting $w(y)$ and $v_{,y}(y)$ firstly. Then $w(y)$ and $v_{,y}(y)$ are calculated using the solution found for $u_{,x}$ and R. After that, the solutions of $w(y)$ and $v_{,y}(y)$ are substituted in equations (12) and (13). The iteration is repeated until the value for bending radius-of-curvature is converged. This is sufficient because for a given R and V_k, $w(y)$ and $v_{,y}(y)$ are determined. The iterative solution process is shown in figure 4 in more details.

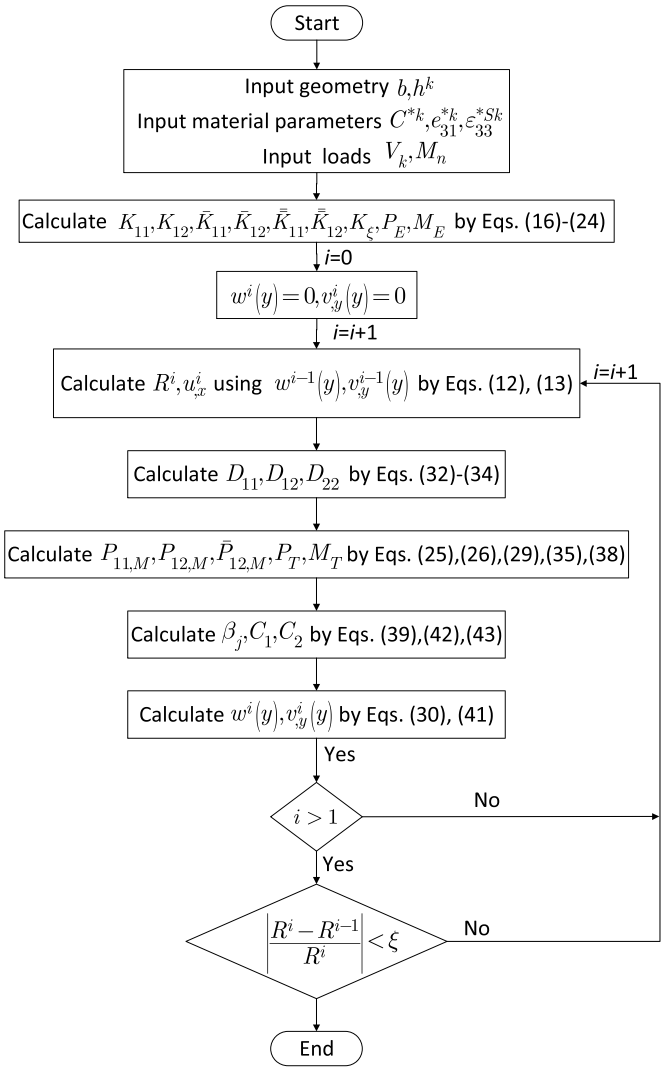

Figure 4. Flow chart for iterative solution of the coupled non-linear equations (12) , (13), (30) and (41) for given voltage and tip bending moment.

3. Results and discussion

In this paper a bimorph and a unimorph configuration are studied, where the bimorph is composed of two layers of 5 μm PZT-5A and the unimorph is made up of the layers of 5 μm glass and 5 μm PZT-5A. We have chosen PZT, because it is a piezoelectric material commonly used in MEMS devices and in commercially available macro-scale devices [32]. The material parameters for PZT5-A were chosen because they are readily available. We considered glass as the structural material because it is widely used in optical structures and has the additional benefit of being isotropic. Hence, we avoid the complications of anisotropy of other relevant materials such as silicon. The material properties are given in table 1.

The convergence of the bending radius-of-curvature is shown in figure 5. In this example the bimorph case is studied, where the width/thickness ratio is taken as 10 and 10 000 for narrow and wide structures, respectively. It is seen that the bending radius-of-curvature converges very fast for both

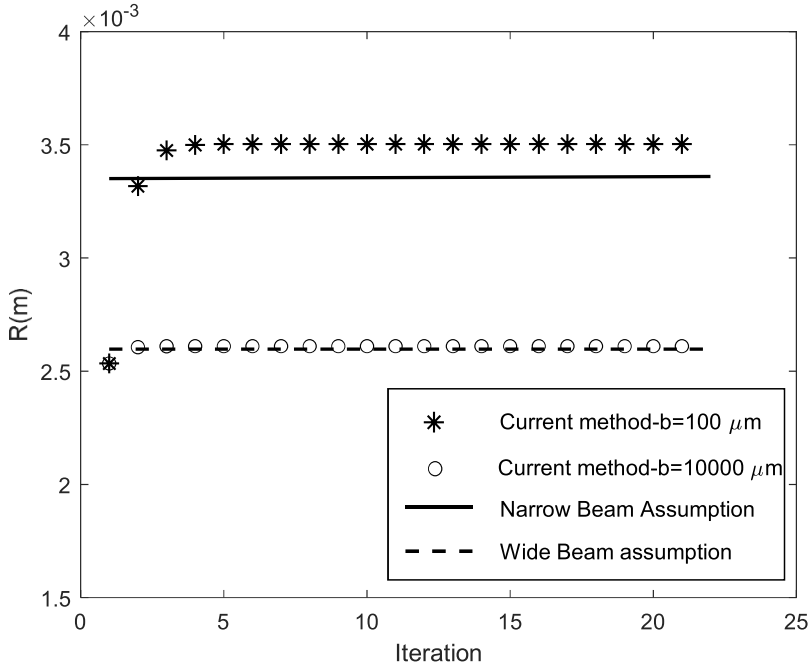

Figure 5. Convergence of the bending radius-of-curvature and comparison of the converged solution with the narrow and wide beam solutions [17].

Table 1. Material properties.

Parameter	Value
PZT-5A	
C_{11} (GPa)	120.34
C_{12} (GPa)	75.18
C_{13} (GPa)	75.09
C_{33} (GPa)	110.87
e_{31} $(\mathrm{C\ m^{-2}})$	−5.35
$\varepsilon^s_{33}/\varepsilon_0$	1900
Glass	
E (GPa)	70
ν	0.27

narrow and wide structures. For the wide structure, the convergence is faster than for the narrow structure because the initial cross-section is closer to the final solution. For the extreme narrow and wide structure cases, results of the current formulation converges to the narrow and wide beam solutions of [17]. However, the current formulation applies to a wide range of widths and provides us with the cross-section deformation.

3.1. Comparison with numerical solution

We use COMSOL Multiphysics® [33] to verify the proposed formulation. Due to the large deformation of the structure along the length, the geometrically non-linear solver option is chosen. The 3D solid element is employed to model the plate structures of 200, 600, 800, and 1500 μm width. The total thickness/width ratio is low enough to satisfy the thin plate assumptions in section 2. The length of all structures are taken at least twice the width to minimize the effects of the support and tip boundary conditions at the mid span [34]. To apply the mechanical moment to the plate, it is extended at the tip by a shell structure and the Solid-Shell connection of Comsol is employed. The deformation of the cross section located at the mid length of the structure from the finite-element solution is compared with the current analytical solution. In order to reduce the finite element method (FEM) computation time, symmetry of the problem is exploited to model half of the structure. Therefore, the comparison of the analytical and FE results is made for half the cross section. We also performed mesh convergence study, and tested against Ashwell's solution [3] for an elastic structure as a benchmark. The FE model is sketched in figure 6.

In the following we will consider different cases. When we have a nonzero voltage across the piezoelectric, we will refer to the situation as electrical actuation. When we have an external bending moment, we will refer to it as mechanical loading. When we have mechanical loading under short-circuit conditions, we will refer to it as pure mechanical loading. The latter is a choice, we could as an alternative have considered mechanical loading under open-circuit conditions.

3.1.1. Electrical actuation only. The first set of verifications is performed on the case of pure electrical actuation by applying voltage on both bimorph and unimorph actuators. The cross-sectional shape of a piezoelectric actuator is affected by two opposite deformations while applying an electric field. First is the result of Poisson's effect because of longitudinal bending, and on the other side there exist bending due to the application of the electric field. The cross-sectional

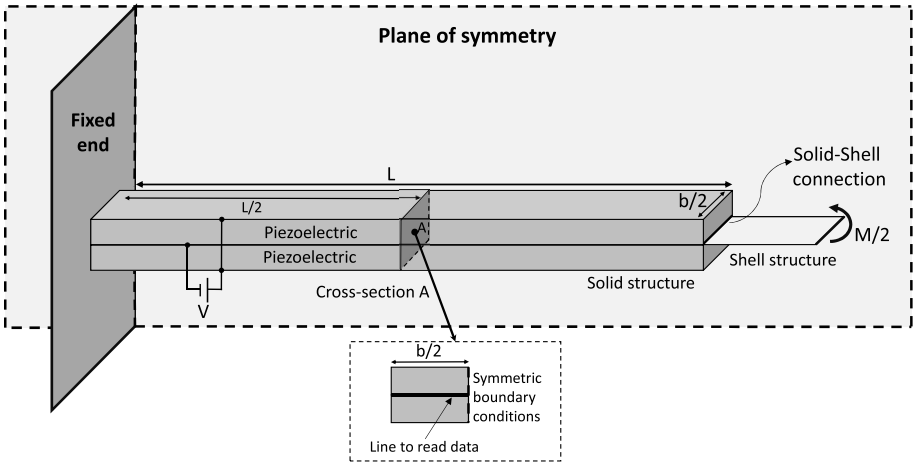

Figure 6. The half symmetric FE model for calculating the cross-section deformation in bending.

deformation of the bimorph actuator is shown in figure 7, in which the voltage of all cases are varied among 3, 15 and 30 V. The consistency of the current analytical solution and the non-linear FE solution results shows that this method is capable of calculating the cross section deformation including anticlastic deformation.

In all cases, the cross sections are deformed in the opposite direction of the anticlastic deformation due to the existence of the moment applied by the electric field. As the width and the voltage of the actuator is increased, the bending radius-of-curvature is decreased for the same electric field, and as the result the Searle parameter is increased. For higher Searle parameters, it is seen that deformation is neutralized at the center of the cross section. Despite higher actuating moment with higher voltage, it is observed that the neutralization force for higher Searle parameter is dominant and in wider structures, the cross section deformation is close to flat, except at the edges.

A comparison of the bending radius-of-curvatures calculated by using the current method, the narrow beam assumption [17] and FEM shows that the current method gives results closer to FEM than the narrow beam solution for the case of bimorph actuator with the width 200 μm. The bending radius-of-curvature of the current formulation and the narrow beam assumptions are calculated as 3.504 and 3.350 mm, respectively.The bending radius-of-curvature from the FE solution is 3.718 mm which is 9.9% and 5.7% higher than the narrow beam assumption and the current method, respectively.

In the case of unimorph actuator, the same behavior as the bimorph actuator is observed. As shown in figure 8, the results of the analytical method well agrees with the results of the FE ones, which verifies the current formulations for the unimorph configuration, as well.

3.1.2. Electrical actuation and mechanical loading. As mentioned in section 1, the cross-section deformation due to pure mechanical loading has been widely studied and verified by the researchers. In the previous section, it was shown that applying an electric field on the piezoelectric layer leads to an electromechanical deformation that is larger than the deformation due to Poisson's effect. In this section, the cross-section deformation is studied by applying both mechanical tip moment and electric field to investigate these two opposite curvatures.

The results of bimorph and unimorph actuators are shown in figures 9 and 10, respectively. The results of both cases are consistent with those from FE, although a bit discrepancy is observed in wider structures. Applying both mechanical loading and electrical actuation, the convergence time of FE solution is dramatically increased in wider structures which is the consequence of solving a highly non-linear problem. As an example, the computational time for the case of the widest bimorph structure $b = 1500$ μm with maximum mechanical loading and electrical actuation voltage is 3 h and 58 min in Comsol, while it takes 2.65 s for our solution on the same computer. Despite the fast solution of the current analytical method, it is possible to predict the behavior of the cross section very well in narrow and wide structures, and even in transition as shown in figures 7–10.

In all cases of pure mechanical loading, the anticlastic curvature is observed. The anticlastic deformation is not neutralized in these examples as the applied mechanical moment is not high enough to increase the Searle parameter. As shown in figures 9 and 10 the cross sections are deformed in different directions by applying either the pure mechanical loading or electrical actuation. Therefore, it is possible to observe flat plate by applying appropriate values of moment and voltage, even in narrow structures. Applying the mechanical and electrical loads simultaneously will result in lower bending radius-of-curvature and higher Searle parameter accordingly. Therefore, the neutralizing force is prominent in wider structures and the deformation is flattened at the central zones in the case of $b = 1500$ μm.

3.2. Cross section flattening

It is seen in the previous section that in a piezoelectric actuator, in addition to the Searle parameter, the relative contributions from mechanical loading and electrical actuation play an

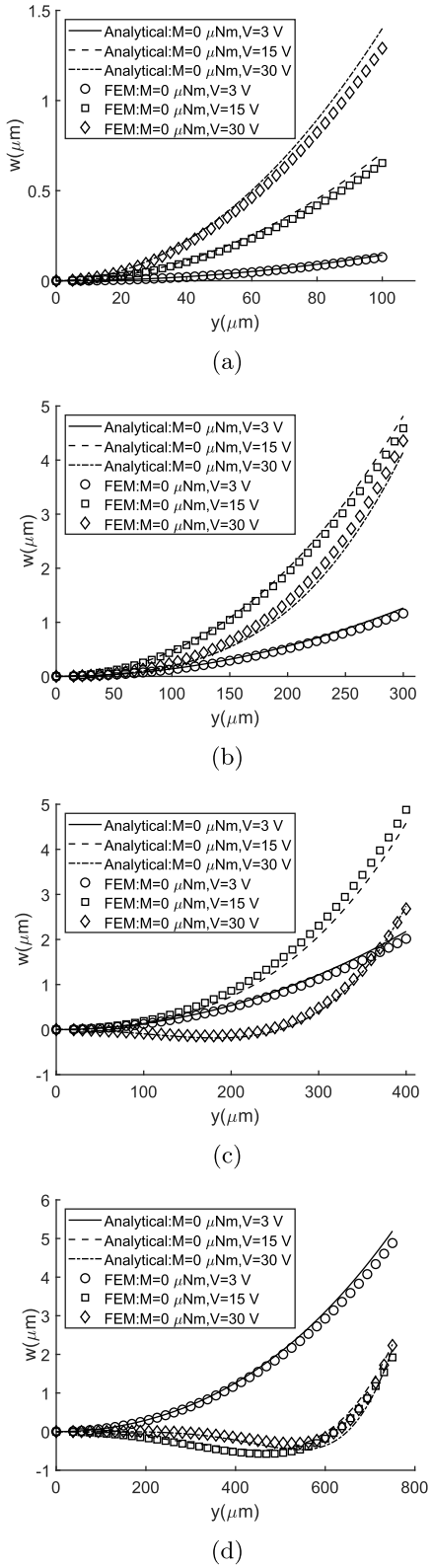

Figure 7. Cross section deformation of the bimorph actuator with electrical actuation and comparison with the FEM: (a) $b = 200$ μm, (b) $b = 600$ μm, (c) $b = 800$ μm, (d) $b = 1500$ μm.

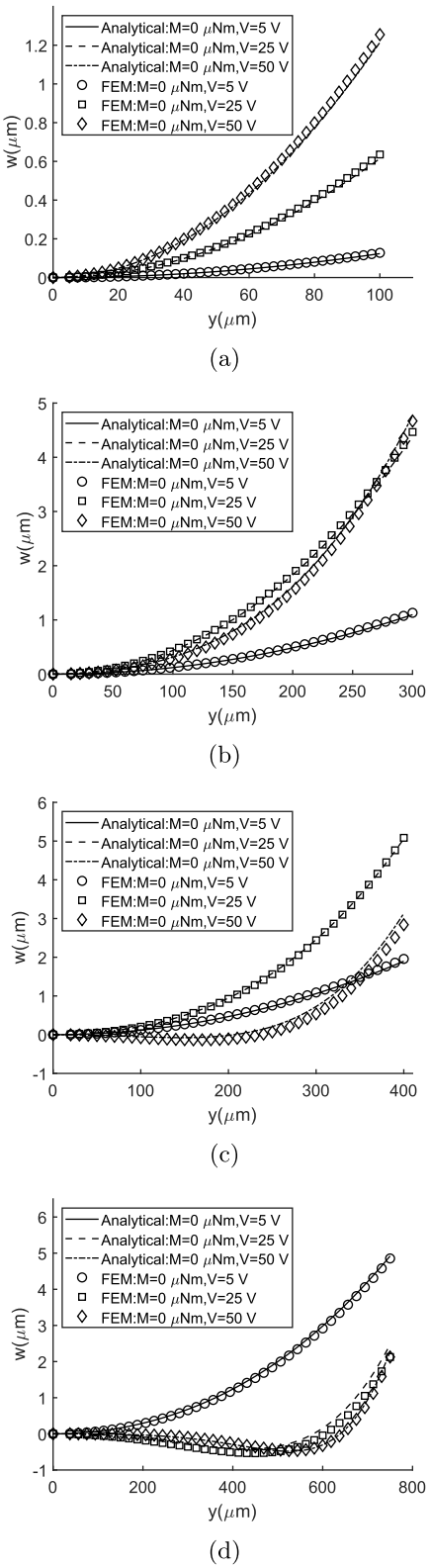

Figure 8. Cross section deformation of the unimorph actuator with electrical actuation and comparison with the FEM: (a) $b = 200$ μm, (b) $b = 600$ μm, (c) $b = 800$ μm, (d) $b = 1500$ μm.

important role in the cross-section deformation. When both contribute to decreasing the bending radius-of-curvature, they oppositely affect the cross-section curvature.

The opposite effect of the electrical and mechanical loadings can help us to find the load values in order to neutralize the cross section deformation. For this purpose an iterative

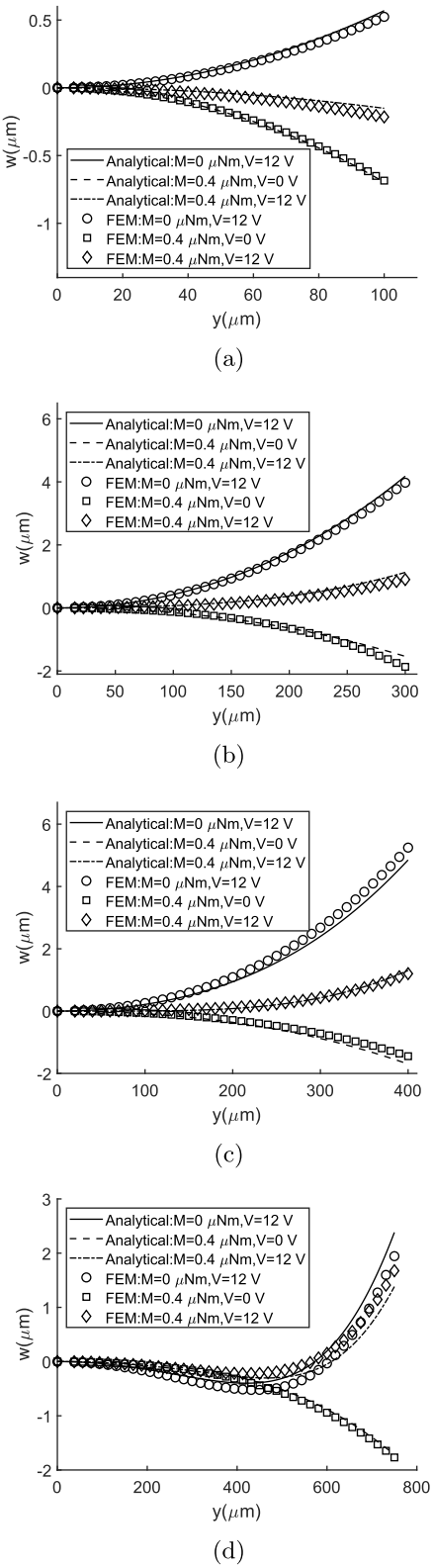

Figure 9. Cross section deformation of the bimorph actuator with electromechanical loading and comparison with the FEM: (a) $b =$ 200 μm, (b) $b = 600$ μm, (c) $b = 800$ μm, (d) $b = 1500$ μm.

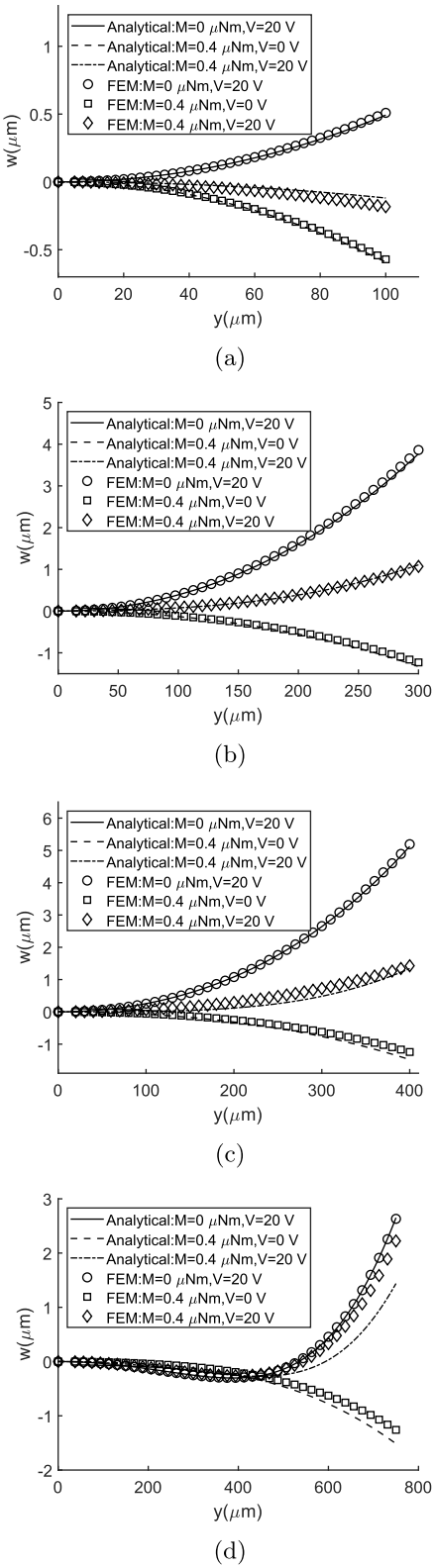

Figure 10. Cross section deformation of unimorph actuator with electromechanical loading and comparison with the FEM: (a) $b =$ 200 μm, (b) $b = 600$ μm, (c) $b = 800$ μm, (d) $b = 1500$ μm.

numerical solution scheme is implemented to find the the bending moment in which $w(0)$ approaches $w(b/2)$ at a given voltage. In this solution scheme, the voltage is kept constant, and the method of bisection is used to find the bending moment that satisfies $w(b/2) - w(0) \approx 0$. The details of the solution procedure are shown in the flow chart of the figure 11.

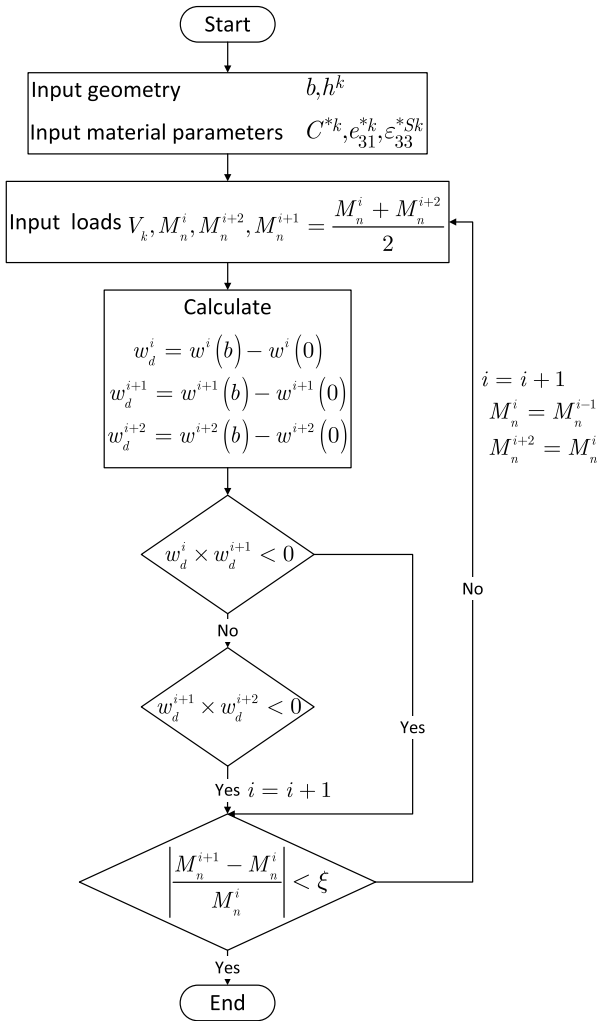

Figure 11. The method of bisection flow chart for finding the neutralization bending moment at a specified actuation voltage.

Figures 12 and 13 show that the cross section deformation can be neutralized by applying both voltage and moment in the bimorph and unimorph actuators, respectively.

In the case of pure mechanical model, any bending moment results in anticlastic deformation, and in a wider structures the anticlastic deformation near the center of the cross section is much smaller than the edges. A piezoelectric actuator behaves in a different way, because it is possible to reduce the deformation in the whole cross section for specific values of applied voltage and mechanical moment. Although it is not possible to make the cross section completely flat as shown in the insets of figures 12 and 13, it can be neglected in comparison with the pure mechanical loading or electrical actuation.

3.3. Searle parameter in piezoelectric actuators

Investigating the moment, voltage and the combination of both loadings indicated that the Searle parameter is an important parameter in cross-section deformation also of piezoelectric actuators. In this section this parameter is studied in more

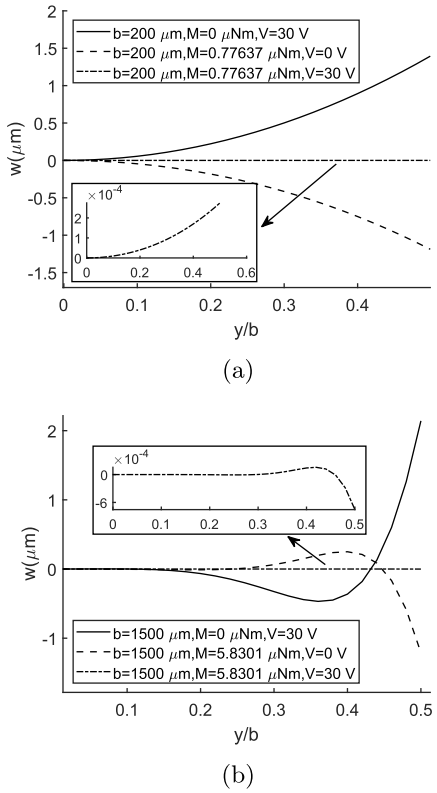

Figure 12. Competing effects of the electrical and mechanical loading on the cross section deformation and cross section neutralization by combining both loadings in bimorph actuators: (a) $b = 200$ μm (b) $b = 1500$ μm.

details in actuators of widths $b = 200$ and $b = 1500$ μm representing narrow and wide structures.

The cross section deformation of structures are shown in figure 14, where the bending radius-of-curvature is kept constant by tuning the voltage and moments for each width. In each case of the narrow and wide structure, the Searle parameter is constant as the radius-of-curvature, width and thickness are the same. In addition to the Searle parameter, the type of loading is an important parameter affecting the cross section deformation as shown in figures 14(a) and (b). As expected, for higher values of Searle parameter the cross section deformation is neutralized near the center of the cross section. We can keep radius-of-curvature of the case $b = 1500$ μm equal to $b = 200$ μm by tuning the applied loading. In figure 15 the radius-of-curvature of the wide structure is 3550 μm, which is the same as the R of the narrow structure in figure 14(a). Comparing both figures, shows the effect of the Searle parameter in neutralization of the wider structure, even with the same radius-of-curvatures. Therefore, the same longitudinal deformation (radius of curvature) might be achieved by applying different combination of loadings, but the cross section deformation is dependent on the Searle parameter and the type of loading.

As the Searle parameter is playing an essential role in the cross section deformation of piezoelectric actuators, we dig into equations to find this parameter. First of all, from

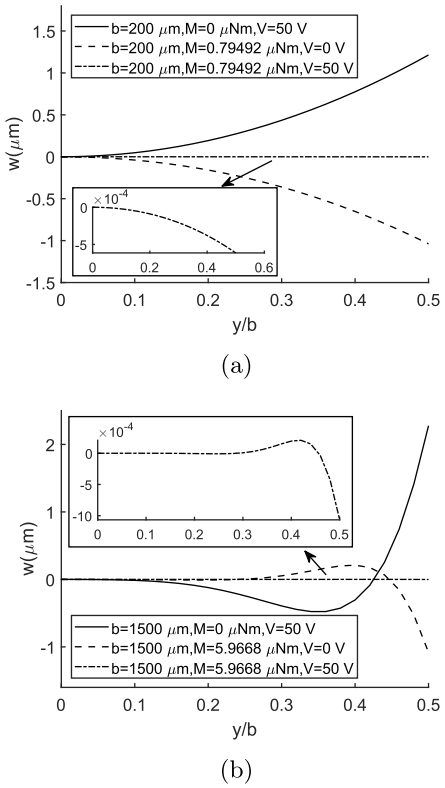

Figure 13. Competing effects of the electrical and mechanical loading on the cross section deformation and cross section neutralization by combining both loadings in unimorph actuators: (a) $b = 200$ μm (b) $b = 1500$ μm.

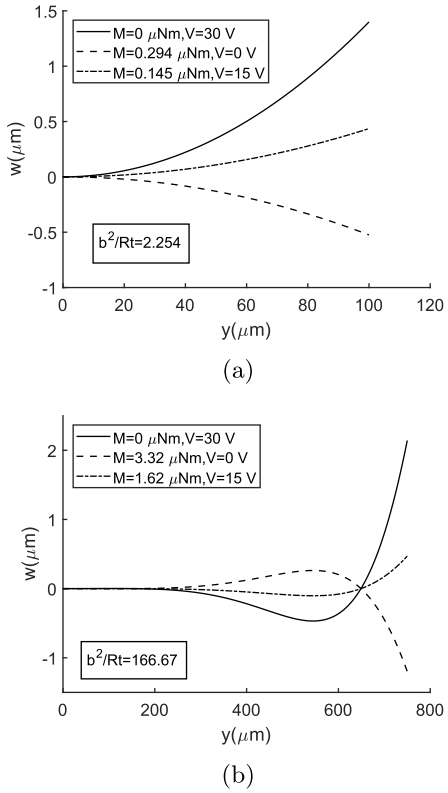

Figure 14. The effect of the type of loading on the cross section deformation of the bimorph actuator with the same bending radius-of-curvature R for the same widths: (a) $b = 200$ μm and $R = 3550$ μm, (b) $b = 1500$ μm and $R = 2700$ μm.

equation (39) α_1 and α_2 are decomposed into the following forms:

$$\alpha_1 = \hat{\alpha}_1\left(C_{ij}^{*k}, e_{mn}^{*k}, \varepsilon_{33}^{*Sk}, H^k\right) \times \frac{1}{\sqrt{Rt}} \tag{52}$$

$$\alpha_2 = \hat{\alpha}_2\left(C_{ij}^{*k}, e_{mn}^{*k}, \varepsilon_{33}^{*Sk}, H^k\right) \times \frac{1}{\sqrt{Rt}}, \tag{53}$$

where $\hat{\alpha}_1$ and $\hat{\alpha}_2$ are functions of the layer stack, material parameters and H^k which is defined as the ratio of each layer's thickness to the structure thickness t. Therefore, for the same layer stack α_1 and α_2 are dependent on the bending radius-of-curvature and the structure thickness. Based on this definition, the cross-section deformation of equation (41) can be rewritten as

$$w(y) = C_1 \sinh\left(\hat{\alpha}_1 \frac{b}{\sqrt{Rt}}\left(\frac{y}{b}\right)\right) \sin\left(\hat{\alpha}_2 \frac{b}{\sqrt{Rt}}\left(\frac{y}{b}\right)\right) + C_2 \cosh\left(\hat{\alpha}_1 \frac{b}{\sqrt{Rt}}\left(\frac{y}{b}\right)\right) \cos\left(\hat{\alpha}_2 \frac{b}{\sqrt{Rt}}\left(\frac{y}{b}\right)\right) - \frac{P_T}{D_{22}}. \tag{54}$$

It is seen in equation (54) that the Searle parameter appears by normalizing the independent variable y by the width b. The equation (54) is similar to that one derived by Ashwell [3].

If the width of an arbitrary actuator is multiplied by a positive value N, to keep the Searle parameter fixed, the bending

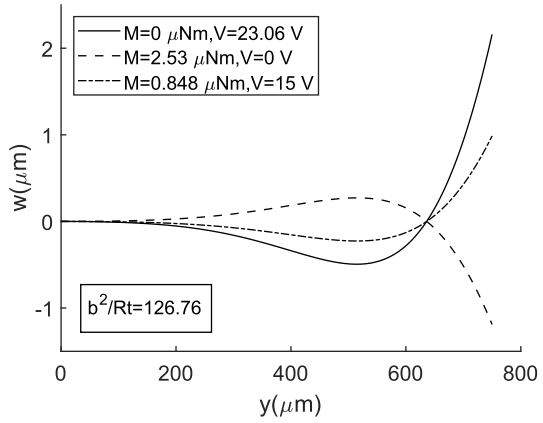

Figure 15. The effect of the type of loading on the cross section deformation of the bimorph actuator with the same radius-of-curvature as figure 14(a), $R = 3550$ μm and $b = 1500$ μm but different Searle parameter.

radius-of-curvature should be multiplied by N^2. Consequently, if the coefficients C_1 and C_2 are unchanged, the cross-section deformation of equation (54) for the width Nb should be the same as the one of the width b. This condition requires P_T and M_T to be unchanged. Regarding equation (12), if R is multiplied by N^2, the axial strain $u_{,x}$ is divided by N^2. Based on equations (35) and (38), fixed values of P_T and M_T forces the value of the voltage divided by N^2. It means that in the case

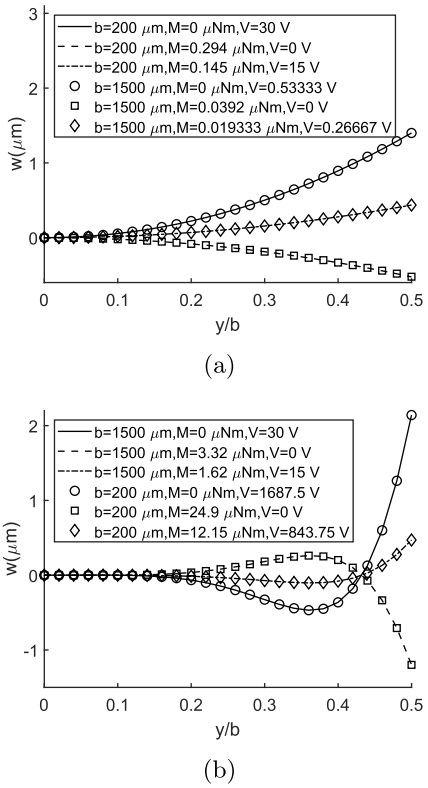

Figure 16. Identical cross-section deformation of bimorph actuators with different widths by applying the load scaling rule (a) Searle parameter = 2.26, (b) Searle parameter = 166.69.

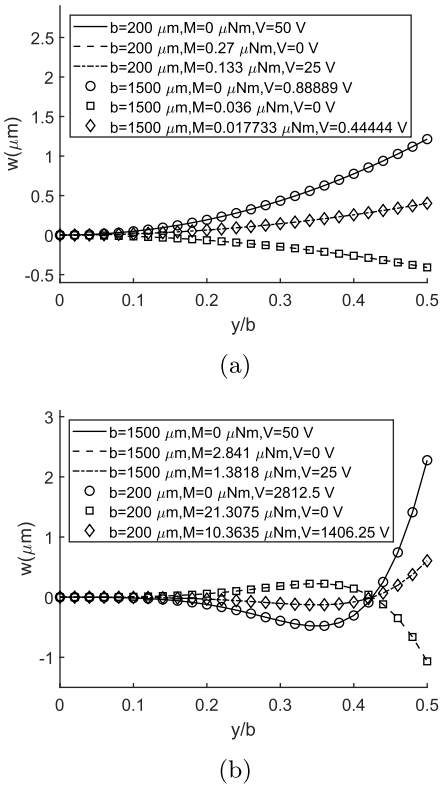

Figure 17. Identical cross section deformation of unimorph actuators with different widths by applying the load scaling rule (a) Searle parameter = 1.95, (b) Searle parameter = 139.06.

of pure electrical actuation, if the width is multiplied by N, the electric potential must be divided by N^2 to get the same shape of cross-section deformation. Referring the equation (13) gives the scaling of the mechanical moment loading $1/N$ for a fixed cross-section deformation. Hence, it is concluded that if the width is multiplied by N, the cross-section deformation of the actuator is unchanged if the mechanical moment M_n and the electric potential V is scaled by $1/N$ and $1/N^2$, respectively. This conclusion is shown for small and large values of Searle parameter in figures 16 and 17 for bimorph and unimorph actuators, respectively. It shows that the deformation of the cross-section versus y/b is unchanged when changing the width provided that the mentioned load scaling rule is obeyed.

4. Conclusion

The cross section deformation of a piezoelectric actuator is affected by the Poisson effect and the electromechanical bending due to the applied voltage. While applying pure mechanical loading, the anticlastic deformation is observed. In contrary, while applying pure electrical actuation, the electromechanical bending in the cross section is dominant and the deformation is opposite the anticlastic deformation. Applying both mechanical and electrical loads, the cross section deformation is induced by both anticlastic deformation and the electromechanical bending simultaneously. Therefore the cross section is affected by these two opposing deformations, and it can be flattened by applying proper values of voltage and mechanical moment.

The same as the mechanical loading, when electrical actuation is applied to a piezoelectric actuator, the deformation of the cross section is neutralized for larger values of Searle parameter. Interestingly, the Searle parameter is an important parameter dictating the cross section deformation in piezoelectric actuators. For the case of combination of electrical and mechanical loadings, a scaling rule is proposed to fix the cross section deformation for different widths of the actuator. If the width is multiplied by N, the voltage and the mechanical moment must be divided by N^2 and N, respectively to keep the cross section deformation versus y/b unchanged. The Searle parameter is also kept fixed by employing this scaling rule.

Data availability statement

The data that support the findings of this study are available from the corresponding author upon reasonable request.

Acknowledgment

This work was supported by the Research Council of Norway through Grant No. 273248.

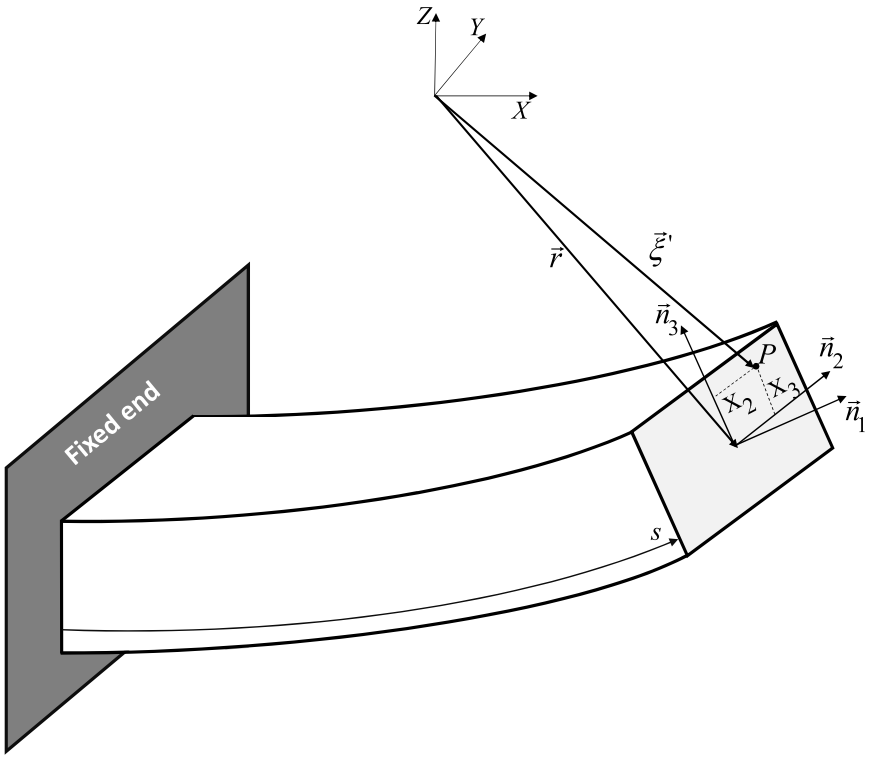

Figure A1. Cross section of the structure after deformation.

Appendix A. Kinematics of the structure

In this section, the kinematics of the structure is used to derive the components of the strain tensor. Figure A1 shows a deformed structure with an orthogonal coordinate system $(\vec{n}_1, \vec{n}_2, \vec{n}_3)$ normal to the cross section at position s along the deformed structure. If the cross section did not deform in bending, the position of an arbitrary point P on the cross section would be

$$\vec{\xi}' = \vec{r} + X_2\vec{n}_2 + X_3\vec{n}_3 \tag{A1}$$

where $\vec{r}$ is the position of the origin of the local coordinate system. To account for the deformation of the cross section, we introduce local displacements (v, w) along $(\vec{n}_2, \vec{n}_3)$ within the cross-section. The position of the point P after deformation is then given by

$$\vec{\xi} = \vec{r} + (X_2 + v)\vec{n}_2 + (X_3 + w)\vec{n}_3. \tag{A2}$$

We can use the vector $\vec{\xi}$ to derive the Green-Lagrange strain tensor as [35]:

$$S_{ij} = \frac{1}{2}\left(\frac{\partial\vec{\xi}}{\partial X_i}\cdot\frac{\partial\vec{\xi}}{\partial X_j} - \delta_{ij}\right), \tag{A3}$$

in which

$$\frac{\partial\vec{\xi}}{\partial X_1} = \frac{ds}{dX_1}\left[\frac{d\vec{r}}{ds} + (X_2 + v)\frac{d\vec{n}_2}{ds} + (X_3 + w)\frac{d\vec{n}_3}{ds}\right] + \frac{\partial v}{\partial X_1}\vec{n}_2 + \frac{\partial w}{\partial X_1}\vec{n}_3, \tag{A4}$$

$$\frac{\partial\vec{\xi}}{\partial X_2} = \left(1 + \frac{\partial v}{\partial X_2}\right)\vec{n}_2 + \frac{\partial w}{\partial X_2}\vec{n}_3, \tag{A5}$$

$$\frac{\partial\vec{\xi}}{\partial X_3} = \frac{\partial v}{\partial X_3}\vec{n}_2 + \left(1 + \frac{\partial w}{\partial X_3}\right)\vec{n}_3. \tag{A6}$$

The vector differentials to s is given as [36]:

$$\frac{d\vec{r}}{ds} = \vec{n}_1 \tag{A7}$$

$$\frac{\partial}{\partial s}\begin{Bmatrix}\vec{n}_1\\ \vec{n}_2\\ \vec{n}_3\end{Bmatrix} = \begin{bmatrix}0 & -\rho_3 & \rho_2\\ \rho_3 & 0 & -\rho_1\\ -\rho_2 & \rho_1 & 0\end{bmatrix}\begin{Bmatrix}\vec{n}_1\\ \vec{n}_2\\ \vec{n}_3\end{Bmatrix} \tag{A8}$$

where ρ_1, ρ_2 and ρ_3 are the twisting curvature around $\vec{n}_1$ and the bending curvature around $\vec{n}_2$ and $\vec{n}_3$, respectively. Due to the loading conditions, ρ_3 and ρ_1 are zero. The axial strain ε_a is introduced as:

$$\varepsilon_a = \frac{ds - dX_1}{dX_1}, \tag{A9}$$

which results in:

$$\frac{ds}{dX_1} = 1 + \varepsilon_a. \tag{A10}$$

Substituting equations (A7), (A8) and (A10) into equation (A4) gives:

$$\frac{\partial\vec{\xi}}{\partial X_1} = (1+\varepsilon_a)\left[(1-\rho_2(X_3+w))\vec{n}_1\right] + \frac{\partial v}{\partial X_1}\vec{n}_2 + \frac{\partial w}{\partial X_1}\vec{n}_3. \tag{A11}$$

Substituting equations (A5), (A6) and (A11) into equation (A3) gives the components of the strain tensor as:

$$S_{11} = \varepsilon_a + \frac{1}{2}\varepsilon_a^2 + \frac{1}{2}(1+\varepsilon_a)^2\{-2\rho_2(X_3+w) + {\rho_2}^2(X_3+w)^2 + \left(\frac{\partial v}{\partial X_1}\right)^2 + \left(\frac{\partial w}{\partial X_2}\right)^2, \tag{A12}$$

$$S_{22} = \frac{\partial v}{\partial X_2} + \frac{1}{2}\left(\frac{\partial v}{\partial X_2}\right)^2 + \frac{1}{2}\left(\frac{\partial w}{\partial X_2}\right)^2, \tag{A13}$$

$$S_{33} = \frac{\partial w}{\partial X_3} + \frac{1}{2}\left(\frac{\partial v}{\partial X_3}\right)^2 + \frac{1}{2}\left(\frac{\partial w}{\partial X_3}\right)^2, \tag{A14}$$

$$S_{12} = \frac{1}{2}(1+\varepsilon_a)\left[\frac{\partial v}{\partial X_1} + \frac{\partial v}{\partial X_1}\frac{\partial v}{\partial X_2} + \frac{\partial w}{\partial X_1}\frac{\partial w}{\partial X_2}\right], \tag{A15}$$

$$S_{13} = \frac{1}{2}(1+\varepsilon_a)\left[\frac{\partial w}{\partial X_1} + \frac{\partial v}{\partial X_1}\frac{\partial v}{\partial X_3} + \frac{\partial w}{\partial X_1}\frac{\partial w}{\partial X_3}\right], \tag{A16}$$

$$S_{23} = \frac{1}{2}\left(\frac{\partial v}{\partial X_3} + \frac{\partial w}{\partial X_2} + \frac{\partial v}{\partial X_2}\frac{\partial v}{\partial X_3} + \frac{\partial w}{\partial X_2}\frac{\partial w}{\partial X_3}\right). \tag{A17}$$

In this section, we have used (X_1,X_2,X_3) to derive the strain tensor, because it is more convenient to follow the indicial notations. Now, we can relate the equations of this section to those ones in section 2 by replacing X_1,X_2,X_3 with $x,y,(z-z_0)$. Assuming small displacement within the cross section as:

$$w = w(x,y), \tag{A18}$$

$$v = v(x,y) - (z-z_0)\frac{\partial w(x,y)}{\partial y}, \tag{A19}$$

neglecting the higher order terms of $\rho_2(X_3+w)$ and ε_a, and in addition making small-strain assumptions, the strain tensor elements become:

$$S_{11} = u_{,x} - \frac{1}{R(x)}((z-z_0)+w), \tag{A20}$$

$$S_{22} = v_{,y} - (z-z_0)\frac{\partial^2 w}{\partial y^2}, \tag{A21}$$

$$S_{33} = 0 \tag{A22}$$

$$S_{12} = \frac{1}{2}\frac{\partial v}{\partial x}, \tag{A23}$$

$$S_{13} = \frac{1}{2}\frac{\partial w}{\partial x}, \tag{A24}$$

$$S_{23} = 0, \tag{A25}$$

where $u_{,x} = \varepsilon_a$ and $\frac{1}{R(x)} = \rho_2$. The shear strains equations (A23) and (A24) vanish, as v and w are not x-dependent.

ORCID iDs

H Salmani https://orcid.org/0000-0002-5726-0327
U Hanke https://orcid.org/0000-0001-9470-767X
E Halvorsen https://orcid.org/0000-0001-6511-9190

References

[1] Lamb H 1891 XXIII. On the flexure of a flat elastic spring *London Edinburgh Dublin Phil. Mag. J. Sci.* **31** 182–8
[2] Searle G F C 1933 *Experimental Elasticity* 2nd edn (Cambridge: Cambridge University Press)
[3] Ashwell D G 1950 The anticlastic curvature of rectangular beams and plates *J. R. Aeronaut. Soc.* **54** 708–15
[4] Kaldor S K and Noyan I C 2002 Differentiating between elastically bent rectangular beams and plates *Appl. Phys. Lett.* **80** 2284–6
[5] Bellow D G, Ford G and Kennedy J S 1965 Anticlastic behavior of flat plates *Experimental Mechanics* **5** 227–32
[6] Stephen R 2001 Swanson, anticlastic effects and the transition from narrow to wide behavior in orthotropic beams *Compos. Struct.* **53** 449–55
[7] Yang W, Larson B C, Ice G E, Tischler J Z, Budai J D, Chung K S and Lowe W P 2003 Spatially resolved Poisson strain and anticlastic curvature measurements in Si under large deflection bending *Appl. Phys. Lett.* **82** 3856–8
[8] Wang J F 2004 Effect of anticlastic curvature on springback of aluminum sheets after the draw-bend test *AIP Conf. Proc.* **712** 820–5
[9] Wang J F, Wagoner R H, Matlock D K and Barlat F 2005 Anticlastic curvature in draw-bend springback *Int. J. Solids Struct.* **42** 1287–307
[10] Kaldor S K and Noyan I C 2005 Flexural loading of rectangular Si beams and plates *Mater. Sci. Eng.* A **399** 64–71
[11] De Bona F, Zelenika S and Munteanu M G 2011 Mechanical properties of microcantilevers: influence of the anticlastic effect *Sensors Actuators* **165** 431–8
[12] Baratta F I 1981 When is a beam a plate? *J. Am. Ceram. Soc.* **64** C–86–C–86
[13] Muralt P 2000 Ferroelectric thin films for micro-sensors and actuators: a review *J. Micromech. Microeng.* **10** 136–46
[14] Elka E, Elata D and Abramovich H 2004 The electromechanical response of multilayered piezoelectric structures *J. Microelectromech. Syst.* **13** 332–41
[15] Weinberg M S 1999 Working equations for piezoelectric actuators and sensors *J. Microelectromech. Syst.* **8** 529–33
[16] Dekkers M, Boschker H, Van Zalk M, Nguyen M, Nazeer H, Houwman E and Rijnders G 2013 The significance of the piezoelectric coefficient d31,eff determined from cantilever structures *J. Micromech. Microeng.* **23** 025008
[17] Nguyen C H, Hanke U and Halvorsen E 2018 Actuation of piezoelectric layered beams with d31 and d33 coupling *IEEE Trans. Ultrason. Ferroelectr. Freq. Control* **65** 815–27

[18] DeVoe D L and Pisano A P 1997 Modeling and optimal design of piezoelectric cantilever microactuators *J. Microelectromech. Syst.* **6** 266–70
[19] Erturk A and Inman D J 2011 *Piezoelectric Energy Harvesting* (New York: Wiley) ch 3, pp 49–96
[20] Curatolo M, La Rosa M and Prestininzi P 2019 On the validity of plane state assumptions in the bending of bimorph piezoelectric cantilevers *J. Intell. Mater. Syst. Struct.* **30** 1508–17
[21] Cioncolini A, Nabawy M R A, Silva-Leon J, O'Connor J and Revell A 2019 An experimental and computational study on inverted flag dynamics for simultaneous wind-solar energy harvesting *Fluids* **4** 87
[22] Orrego S, Shoele K, Ruas A, Doran K, Caggiano B, Mittal R and Kang S H 2017 Harvesting ambient wind energy with an inverted piezoelectric flag *Appl. Energy* **194** 212–22
[23] Wang J, Nabawy M R A, Cioncolini A and Revell A 2019 Solar panels as tip masses in low frequency vibration harvesters *Energies* **12** 1–20
[24] Song J, Zhao G, Li B and Wang J 2017 Design optimization of PVDF-based piezoelectric energy harvesters *Heliyon* **3** e00377
[25] Timoshenko S and Goodier J N 1969 Engineering mechanics series *Theory of Elasticity* (New York: McGraw-Hill)
[26] IEEE standard on piezoelectricity 1988 *ANSI/IEEE Std 176-1987* 0_1-
[27] Tiersten H F 1969 *Linear Piezoelectric Plate Vibrations: Elements of the Linear Theory of Piezoelectricity and the Vibrations Piezoelectric Plates* (Boston: Springer) (https://doi.org/10.1007/978-1-4899-6453-3)
[28] Ugural A C 1981 *Stresses in Plates and Shells* (New York: McGraw-Hill) ch 1, p 1
[29] Benjeddou A, Trindade M A and Ohayon R 1997 A unified beam finite element model for extension and shear piezoelectric actuation mechanisms *J. Intell. Mater. Syst. Struct.* **8** 1012–25
[30] Tiersten H F 1967 Hamilton's principle for linear piezoelectric media *Proc. IEEE* **55** 1523–4
[31] Bathe K-J 2014 *Finite Element Procedures* 2nd edn (Englewood Cliffs: Prentice Hall Pearson Education)
[32] Piezo Systems Inc (available at: www.piezo.com)
[33] Comsol multiphysics v. 5.4. COMSOL AB, Stockholm, Sweden (available at: www.comsol.com)
[34] Choi I and Horgan C O 1977 Saint-Venant's principle and end effects in anisotropic elasticity *J. Appl. Mech.* **44** 424–30
[35] Michael Lai W, Rubin D and Krempl E 2010 *Introduction to Continuum Mechanics* 4th edn (Boston: Butterworth-Heinemann) pp 69–153
[36] Nayfeh A H and Pai P F 2004 *Linear and Nonlinear Structural Mechanics* (New York: Wiley) ch 4, pp 171–265